Simulation of frequency- and wave-vector-resolved femtosecond resonant x-ray emission of molecular chains

Satoshi Tanaka[1,2] and Shaul Mukamel[1]
[1]*Department of Chemistry, University of Rochester, Rochester, New York 14627*
[2]*College of Integrated Arts and Sciences, Osaka Prefecture University, Sakai 599-8531, Japan*
(Received 16 March 2001; published 13 August 2001)

X-ray fluorescence signals that provide a localized (atom-specific) probe of core excitations in molecules are calculated for a one-dimensional chain of atoms. The relative and the translational motions of electron-hole pairs are clearly separated in real space and may be directly probed by the frequency and wave-vector dependence of the signals.

DOI: 10.1103/PhysRevA.64.032503 PACS number(s): 33.20.Rm, 42.50.Hz, 78.47.+p

I. INTRODUCTION

The dynamics of electronic excitations in assemblies of coupled molecules (aggregates, light-harvesting molecules, dendrimers) [1–5] and nanostructure semiconductors (quantum dots, wells, and wires) [6–11] have been extensively studied by ultrafast optical nonlinear spectroscopies. Geometric confinement of excitons often gives rise to a large enhancement of optical nonlinearities resulting from the increased binding energy and oscillator strength. Nonlinear spectroscopy in the optical region provides detailed information on the dynamics of a confined excitons. However, optical techniques can only create a spatially homogeneous (uniform) distribution of excitons, since the optical wavelength is longer than the exciton spatial coherence length. In order to investigate exciton dynamics in confined systems, it is necessary to probe separately the relative and the translational motion of the electron-hole pairs in real space. This may be possible using time- and frequency-resolved x-ray emission spectroscopy. In addition the dipole approximation that applies for optical excitations often implies selection rules that make only a few excitons available. X-ray excitations are not subjected to the selective rules and can probe the entire exciton band.

Recent advances in the development of the intense femtosecond coherent x-ray sources have opened up new possibilities of ultrafast spectroscopy in x-ray region. X-ray pulses as short as 300 fs have been reported so far [12], but much shorter 10^{-18} s pulses are possible. In addition to their temporal resolution, x rays have a high spatial resolution, stemming from their 100 Å to 1 Å wavelength. X-ray pulses have therefore the unique capacity to directly probe the dynamics of elementary excitations in materials, such as excitons, polaritons, and polarons, as well as nuclear motions in real time and space [13–16].

One notable characteristic of x-ray excitation is its high selectivity achieved by tuning the wavelength to a particular core-state resonance. Local electronic structure and bonding around an excited atom have thus been investigated by various types of core-level spectroscopies, including x-ray photoemission [17–20], extended x-ray absorption fine structure [21,22], x-ray absorption near edge structure [23], and x-ray emission (fluorescence) [24]. The creation of a core hole by an incident x-ray photon induces a significant change of the electronic states and nuclear motions that tend to screen the core hole potential [25–27], giving rise to shake-up satellite or vibrational sidebands in x-ray absorption and photoemission spectra are direct evidence for these effects [20,23]. Core-level spectroscopies have therefore become a powerful tool for investigating electronic states of strongly correlated materials, including $3d$ transition metals and rare-earth compounds [19,20].

The relaxation dynamics and nuclear motions in core excited states have direct signatures in x-ray emission spectrum [27–31]. Frequency domain resonant x-ray emission studies were carried out in crystals [32–37], gas molecules [38,40], polymers [41], and surface adsorbates [39]. Frequency domain resonant x-ray emission has been calculated using the Kramers-Heisenberg formula [42–48]. Cederbaum and co-workers had employed a time-dependent wave packet representation for the resonant x-ray emission spectrum of molecules [29,30,49]. Gel'mukhanov and co-workers have also used the time-dependent form of the Kramers-Heisenberg formula to calculate resonant x-ray emission spectra of molecules and study the nuclear relaxation dynamics upon core excitations [31,50,51]. Recently they have computed a theory for the time- and frequency-resolved x-ray emission spectrum using equations of motion for the density matrix, and calculated the spectrum for a simple three-level systems coupled to molecular vibrations [52].

We have recently formulated the theory of nonlinear x-ray spectroscopy in terms of nonlinear response functions [53], which provide a systematic approach for computing the nonlinear response to any desired order in the incoming fields. The *Liouville space pathways* for the nonlinear response provide an intuitive picture for time-resolved spectroscopies, since they establish a connection between the time evolution of the density matrix and the observed signal. In this paper we apply this formalism towards the calculation of the time and frequency-resolved emission spectrum (TFXES) in a three-band model for a one-dimensional atomic chain. The model is presented in Sec. II. Formal expressions for TFXES are given in Sec. III. Numerical calculations are shown in Sec. IV, and the results are discussed in Sec. V.

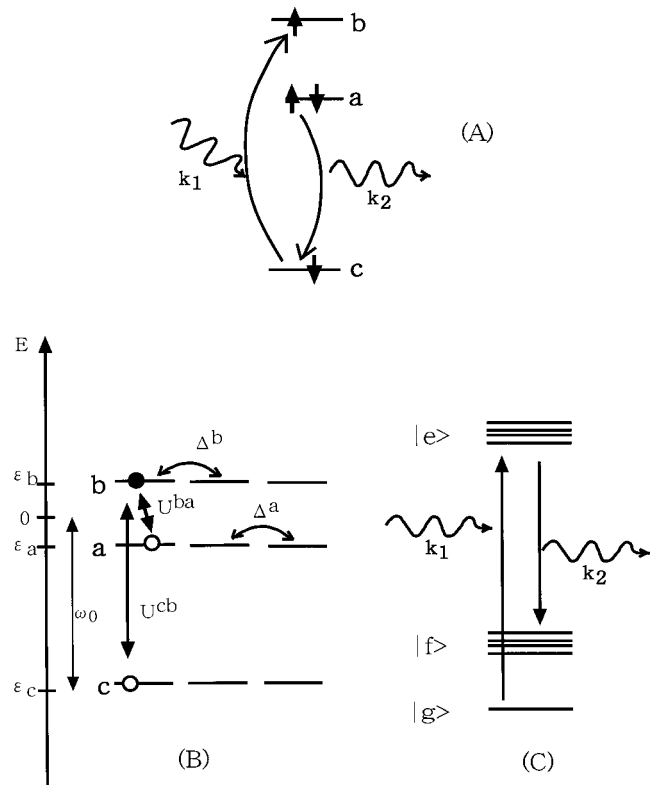

FIG. 1. (a) X-ray scattering process for a three-atomic-orbital model, (b) interactions between the atomic levels, and (c) the level schemes for the global eigenstates of molecules consisting N atoms. ϵ_c, ϵ_b, and ϵ_a are the energies of the core, unoccupied, and occupied valence orbitals, respectively. $\omega_0 \equiv -\epsilon_c$ is a reference energy. Δ^b and Δ^a are the transfer integrals between the b and a atomic orbitals, respectively. The Coulomb interactions between the core hole and the excited electron, and between the valence hole and the excited electron are denoted U^{cb} and U^{ba}, respectively. In (c), the global eigenstates for the ground, core-excited, and the final (optically-valence-excited) states are represented by $|g\rangle$, $|e\rangle$, and $|f\rangle$, respectively.

II. THE CORE-EXCITON MODEL

In a resonant x-ray emission process from a single atom, the incoming x-ray beam excites an electron from a core orbital c to an unoccupied orbital b, and the x-ray photon emission subsequently takes place when an electron moves from a different occupied valence orbital a to the core orbital c. The core excited state has an electron in orbital b and a core-hole in orbital c. Following the x-ray photon emission, an electron and a hole are left in orbitals b and a, respectively. The process [Fig. 1(a)] thus involves at least three orbitals, with energies ϵ_a, ϵ_b, and ϵ_c, respectively.

We denote the Fermi creation (annihilation) operator of the electron in the orbital b as $b^\dagger(b)$, and the creation (annihilation) operator of the hole in the orbitals a and c, by $a^\dagger(a)$ and $c^\dagger(c)$, respectively. For clarity, we neglect the multiplet couplings between the core hole and excited electron, and between the valence hole and the excited electron, so that we can ignore the spin degrees of freedom. Our model consists of a linear chain of N identical atoms [Fig. 1(b)] described by the Hamiltonian

$$
\begin{aligned}
H = & -\sum_{l=0}^{N-1} \epsilon_c c_l^\dagger c_l + \sum_{l=0}^{N-1} \epsilon_b b_l^\dagger b_l - \sum_{l=0}^{N-1} \epsilon_a a_l^\dagger a_l \\
& - \sum_{lm=0}^{N-1} \Delta_{lm}^b b_l^\dagger b_m + \sum_{lm=0}^{N-1} \Delta_{lm}^a a_l^\dagger a_m \\
& - \sum_{ll'mm'} U_{l'm';lm}^{cb} b_{l'}^\dagger c_{m'}^\dagger c_m b_l \\
& - \sum_{ll'mm'} U_{l'm';lm}^{ba} a_{l'}^\dagger b_{m'}^\dagger b_m a_l . \qquad (1)
\end{aligned}
$$

The first three terms in the right-hand side represent the three atomic orbitals of the N sites. The following two terms represent the electron and hole exchange between these orbitals, where Δ_{lm}^j denotes the transfer integral of orbitals $j(=b,a)$ between the lth and mth sites. We adopt the tight-binding Hamiltonian for the occupied and unoccupied valence orbitals, i.e., we only take into account the nearest-neighbor transfer between b's (Δ^b) and a's (Δ^a) orbitals. We also neglect the transfer between the core orbitals c, because it is usually very small, i.e., the transfer between C $1s$ core orbitals has been estimated ~ 50 meV in C_2H_2, whereas the other parameters have magnitudes of ~ 1 eV. [54] The last two terms represent the Coulomb interactions between the core hole and the excited electron, (U^{cb}), and between the valence hole and the excited electron (U^{ba}). We further assume equal spacing a_0 between neighboring atoms with the periodic boundary condition.

We shall denote the relevant many-electron eigenstates of this Hamiltonian as the ground $|g\rangle$, core-excited $|e\rangle$ and final states $|f\rangle$. [Fig. 1(c)] $|e\rangle$ are obtained by diagonalizing the Hamiltonian using the basis set:

$$
|l_h m_e\rangle_c = c_l^\dagger b_m^\dagger |g\rangle . \qquad (2)
$$

$|f\rangle$ are obtained similarly by diagonalizing the Hamiltonian with the basis set:

$$
|l_h m_e\rangle_v = a_l^\dagger b_m^\dagger |g\rangle . \qquad (3)
$$

Similar Hamiltonians are used for describing the optical response of semiconductors [7] and conjugated molecules [55]. For simplicity, in this paper, we neglect the exchange Coulomb interaction, setting $U_{l'm';lm}^j = 0$ unless $l = l'$ and $m = m'$. We assume the Ohno model for Coulomb interaction

$$
U_{lm;lm}^j = \frac{U^j}{\sqrt{1 + [a_0(l-m)/\epsilon^2 U^j]^2}}, \quad (j = cb, ba), \qquad (4)
$$

where ϵ represents a screening range of the long-range Coulomb interaction. The Ohno model interpolates between the on site repulsion U^j of the Hubbard model and the long range Coulomb and can describe exciton binding.

III. THE TIME- AND FREQUENCY-RESOLVED X-RAY EMISSION SPECTRUM

We consider an experiment whereby the system is irradiated by the x-ray pump pulse and the spontaneously emitted x-ray photon with scattering wave vector $\mathbf{q}_s$ is detected using time and frequency gates. Even though the signal intensity is proportional to the incident x-ray intensity and the technique is strictly speaking linear, the process can be formulated as a nonlinear third-order response [53,56]. The same formulation also holds for time-resolved x-ray diffraction [53].

The emitted x-ray mode should be treated quantum mechanically while the incident beam is treated classically. The vector potential is thus expanded as

$$A(\mathbf{r},t)=A_1(t+\tau)\exp[i(\mathbf{k}_1\mathbf{r}-\omega_1 t)]+A_2(t)\times\exp[i(\mathbf{k}_2\mathbf{r}-\omega_2 t)]+\text{c.c.} \tag{5}$$

where A_1 is the classical incident x-ray field envelope, and the emitted x-ray mode is described by the operator

$$A_2=c\left(\frac{\boldsymbol{\epsilon}_{\mathbf{q}_2}}{\omega_2}\right)B_2,\quad A_2^*=c\left(\frac{\boldsymbol{\epsilon}_{\mathbf{q}_2}}{\omega_2}\right)B_2^\dagger, \tag{6}$$

where B_2 ($B_2^\dagger$) denotes the annihilation (creation) operator of the emitted x-ray photon.

The operator representing the photon emission rate is

$$\mathcal{N}_s\equiv\frac{d}{dt}B_2^\dagger B_2=\frac{i}{\hbar}[H_{int},B_2^\dagger B_2], \tag{7}$$

and the photon emission rate with the energy ω_2 at time t is given by $\mathrm{Tr}[\mathcal{N}_s\rho_T(t)]$, where $\rho_T(t)$ denotes a density matrix for the whole system including the material and the radiation field. The time-gated fluorescence obtained by mixing the signal with the time-gating field $A_t(t)$ is calculated in Appendix A:

$$\begin{aligned}F(\mathbf{k}_1,\mathbf{k}_2;\tau)=2\,\mathrm{Re}\sum_{ll_1l_2l_3}\int_{-\infty}^{\infty}dt\int_0^\infty dt_3\int_0^\infty dt_2\int_0^\infty dt_1\{&A_1(t+\tau-t_1-t_2-t_3)A_1^*(t+\tau-t_2-t_3)A_t(t-t_3)A_t^*(t)\\&\times\exp[i\omega_1t_1+i\omega_2t_3]\exp[i\mathbf{k}_1\cdot(\mathbf{R}_{l_1}-\mathbf{R}_{l_2})]\exp[i\mathbf{k}_2\cdot(\mathbf{R}_{l_3}-\mathbf{R}_l)]R_1(l;l_3l_2l_1t_3t_2t_1)\\&+A_1^*(t+\tau-t_1-t_2-t_1)A_1(t+\tau-t_2-t_3)A_t(t-t_3)A_t^*(t)\exp[-i\omega_1t_1+i\omega_2t_3]\exp[-i\mathbf{k}_1\cdot(\mathbf{R}_{l_1}-\mathbf{R}_{l_2})]\\&\times\exp[-i\mathbf{k}_2\cdot(\mathbf{R}_l-\mathbf{R}_{l_3})]R_2(l;l_3l_2l_1t_3t_2t_1)+A_1^*(t+\tau-t_1-t_2-t_3)A_1(t+\tau-t_3)A_t(t-t_2-t_3)A_t^*(t)\\&\times\exp[-i\omega_1t_1-i(\omega_1-\omega_2)t_2+i\omega_2t_3]\exp[-i\mathbf{k}_1(\mathbf{R}_{l_1}-\mathbf{R}_{l_3})]\exp[-i\mathbf{k}_2(\mathbf{R}_l-\mathbf{R}_{l_2})]R_3(l;l_3l_2l_1t_3t_2t_1)\}.\end{aligned} \tag{8}$$

The correlation functions $\mathbf{R}_j$ are represented by summations over of the global (many-electron) eigenstates:

$$R_1=\sum_{gfee'}P(g)j_{fe}(l)j_{fe'}^*(l_3)j_{e'g}^*(l_2)j_{eg}(l_1)\times I_{ef}(t_3)I_{ee'}(t_2)I_{eg}(t_1), \tag{9a}$$

$$R_2=\sum_{gfee'}P(g)j_{fe}(l)j_{fe'}^*(l_3)j_{eg}(l_2)j_{e'g}^*(l_1)\times I_{ef}(t_3)I_{ee'}(t_2)I_{ge'}(t_1), \tag{9b}$$

$$R_3=\sum_{gfee'}P(g)j_{fe}(l)j_{eg}(l_3)j_{fe'}^*(l_2)j_{e'g}^*(l_1)\times I_{ef}(t_3)I_{gf}(t_2)I_{ge'}(t_1). \tag{9c}$$

where $P(g)$ is the ground state population. The matrix elements of the current density between the many-electron eigenstates, $j_{\xi\eta}$ ($\xi,\eta=g,e,e',f$), are given in Appendix A. $I_{\xi\eta}(t)$ is an auxiliary function

$$I_{\xi\eta}(t)\equiv\theta(t)\exp[-i\omega_{\xi\eta}t-\Gamma_{\xi\eta}t], \tag{10}$$

where $\omega_{\xi\eta}\equiv(\epsilon_\xi-\epsilon_\eta)/\hbar$ is the transition frequency. $\Gamma_{\xi\eta}$ is the relaxation rate defined by

$$\Gamma_{\xi\eta}=\frac{1}{2}(\gamma_\xi+\gamma_\eta)+\hat{\Gamma}_{\xi\eta}, \tag{11}$$

where γ_ξ and γ_η are the inverse lifetimes of the ξ and η states, and $\hat{\Gamma}_{\xi\eta}$ is the pure dephasing rate for the $\xi\eta$ transition. Since the Hamiltonian [Eq. (1)] is diagonal with respect to the core orbitals C_l, we have in Eq. (9) $R_1\propto\delta_{ll_1}\delta_{l_2l_3}$,$R_2\propto\delta_{ll_2}\delta_{l_1l_3}$,$R_3\propto\delta_{ll_3}\delta_{l_1l_2}$.

In our numerical simulations we have used Gaussian pulses

$$A_j(t)=\frac{1}{\delta_j\sqrt{2\pi}}\exp\left[-\frac{t^2}{2\delta_j^2}\right]\quad(j=1,t). \tag{12}$$

We further assume that $\gamma_g=\gamma_f=0$ and $\hat{\Gamma}_{eg}=\hat{\Gamma}_{ee'}=\hat{\Gamma}_{ef}=0$.

Substituting Eq. (12) into Eq. (8), the gated signal is finally recast in the following form. (See Appendix B for details.)

$$F(\mathbf{k}_1,\mathbf{k}_2;\tau)=2\pi^{-3/2}\frac{1}{\delta_1\delta_t\sqrt{\delta_1^2+\delta_t^2}}$$
$$\times\mathrm{Re}\sum_{gee'f}P(g)J_{fe;eg}(\mathbf{q}_s)J^*_{fe';e'g}(\mathbf{q}_s)$$
$$\times\int_{-\infty}^{\infty}dx\int_0^{\infty}dy\int_{|x-y|}^{\infty}dz$$
$$\times\exp\Bigg[-\frac{x^2}{\delta_1^2}-ix$$
$$\times\{2\omega_1-(\omega_e+\omega_{e'}-2\omega_g)\}\Bigg]$$
$$\times\exp\Bigg[-\frac{y^2}{\delta_t^2}+iy\{2\omega_t-(\omega_e+\omega_{e'}-2\omega_f)\}\Bigg]$$
$$\times\exp\Bigg[-\frac{1}{\delta_1^2+\delta_t^2}(z-\tau)^2$$
$$-i(\omega_e-\omega_{e'})z-\Gamma z\Bigg]. \tag{13}$$

where

$$J_{fe;eg}(\mathbf{q}_s)\equiv\sum_l j_{fe}(l)j_{eg}(l)\exp(-i\mathbf{q}_s\cdot\mathbf{R}_l), \tag{14}$$

$\mathbf{q}_s\equiv\mathbf{k}_2-\mathbf{k}_1$ is a scattering wave vector and $\gamma_e=\gamma_{e'}=\Gamma$. It should be noted that the above formula may be also obtained using a second-order perturbative calculation of the wave function. In the absence of pure dephasing ($\hat{\Gamma}=0$), a destructive interference takes place, canceling the fluorescence Liouville space pathways: The total emission is then of the Raman type [56]. Once dephasing processes are incorporated, the system is no longer in a pure state and may not be represented by wavefunction; the density operator description is then essential. In this case, we need to evaluate each Liouville space paths using Eqs. (B1).

If the incident x-ray pulse and the time-gated detection pulse are temporarily well separated, the triple integrations in Eq. (13) can be factorized into three one-dimensional integrals, and the TFXES signal is finally given by

$$F(\mathbf{k}_1,\mathbf{k}_2;\tau)=\sum_{gee'f}P(g)J_{fe;eg}(q)J^*_{fe';e'g}(q)$$
$$\times\exp\Bigg[-\frac{\delta_1^2}{4}\{2\omega_1-(\omega_e+\omega_{e'}-2\omega_g)\}^2\Bigg]$$
$$\times\exp\Bigg[-\frac{\delta_t^2}{4}\{2\omega_t-(\omega_e+\omega_{e'}-2\omega_f)\}^2\Bigg]$$
$$\times\exp\Bigg[-\frac{1}{4}(\delta_1^2+\delta_t^2)(\omega_e-\omega_{e'})^2$$
$$+\frac{1}{4}(\delta_1^2+\delta_t^2)\Gamma^2-\Gamma\tau\Bigg]\exp\Bigg[-i(\omega_e-\omega_{e'})$$
$$\times\Bigg\{\tau-\frac{1}{2}(\delta_1^2+\delta_t^2)\Gamma\Bigg\}\Bigg]. \tag{15}$$

All calculations reported below were carried out using Eq. (15).

IV. NUMERICAL CALCULATIONS

We assumed $\epsilon_b=8$ eV, $\epsilon_a=-8$ eV, $\Delta^b=-2$ eV, and $\Delta^a=1.5$ eV, $\Gamma=32$meV, and took $-\epsilon_c$ as the energy origin. These are typical parameters for conjugated molecules [57].

We first present calculations for $N=2$. This case is simple yet useful for illustrating the information contained in TFXES. Because of inversion symmetry, the total electronic Hilbert space is partitioned into a symmetric (gerade, g) and antisymmetric (ungerade, u) subspaces. The symmetrized states for the valence-excited state are represented by the site basis shown in Eq. (3):

$$|j=0,g(u)\rangle_v\equiv\frac{1}{\sqrt{2}}\{|0_h0_e\rangle_v\pm|1_h1_e\rangle_v\},$$
$$|j=1,g(u)\rangle_v\equiv\frac{1}{\sqrt{2}}\{|0_h1_e\rangle_v\pm|1_h0_e\rangle_v\}, \tag{16}$$

where $+$ $(-)$ denote g (u) subspaces. $j=0,1$ is used to classify the basis involved in the same subspace, and represents the relative hole-electron separation, i.e., a hole and an electron is located in the same site in $|0,g(u)\rangle_v$, while they are separated in $|1,g(u)\rangle_v$. The relative motion is represented by j and a translational motion of the pair is represented by g or u.

Using this basis set $\{|0,g\rangle_v,|1,g\rangle_v,|0,u\rangle_v,|1,u\rangle_v\}$ the valence excited state Hamiltonian is

$$H=\begin{bmatrix}\epsilon_b-\epsilon_a-U^{ba} & \Delta^b-\Delta^a & 0 & 0\\ \Delta^b-\Delta^a & \epsilon_b-\epsilon_a & 0 & 0\\ 0 & 0 & \epsilon_b-\epsilon_a-U^{ba} & \Delta^b+\Delta^a\\ 0 & 0 & \Delta^b+\Delta^a & \epsilon_b-\epsilon_a\end{bmatrix}. \tag{17}$$

The symmetric $|e\rangle$ eigenstates are

$$|\alpha,g\rangle_v=\cos\theta|0,g\rangle_v+\sin\theta|1,g\rangle_v,$$
$$|\beta,g\rangle_v=-\sin\theta|0,g\rangle_v+\cos\theta|1,g\rangle_v, \tag{18}$$

with energies

$$E_{\alpha(\beta),g}=\epsilon_b-\epsilon_a-\frac{1}{2}\{U^{ba}\pm\sqrt{(U^{ba})^2+4\Delta_g^2}\}, \tag{19}$$

where $\Delta_g \equiv \Delta^b - \Delta^a$, and $+(-)$ corresponds to the state $\alpha(\beta)$. We further have

$$\cos 2\theta = \frac{U^{ba}/2}{\sqrt{(U^{ba})^2/4 + \Delta_g^2}},$$

$$\sin 2\theta = \frac{-\Delta_g}{\sqrt{(U^{ba})^2/4 + \Delta_g^2}}. \tag{20}$$

The antisymmetric eigenstates are similarly obtained by

$$|\alpha,u\rangle_v = \sin\theta|0,u\rangle_v + \cos\theta|1,u\rangle_v,$$

$$|\beta,u\rangle_v = -\cos\theta|0,u\rangle_v + \sin\theta|1,u\rangle_v, \tag{21}$$

with energies

$$E_{\alpha(\beta),u} = \epsilon_b - \epsilon_a - \frac{1}{2}\{U^{ba} \pm \sqrt{(U^{ba})^2 + 4\Delta_u^2}\}, \tag{22}$$

where $\Delta_u \equiv \Delta^b + \Delta^a$, and $+(-)$ sign takes for the state $\alpha(\beta)$. The core-excited state Hamiltonian is obtained by replacing $\epsilon_b - \epsilon_a$ with ϵ_b and U^{ba} with U^{cb}, and taking $\Delta^a = 0$. The core excited eigenstates can be represented similarly. It should be noted that as the Coulomb interaction is increased, $E_\alpha - E_\beta$ increases, and $|\alpha\rangle$ tends to represent a localized Frenkel exciton state, where the hole and electron are confined to the same site, while $|\beta\rangle$ represents a dissociated exciton (free electron-hole pair).

The energy level-scheme for the $|e\rangle$ and $|f\rangle$ states is depicted in Fig. 2. In $|e\rangle$, $|\alpha\rangle_c$ and $|\beta\rangle_c$ are doubly degenerate since the transfer between the core states was neglected. In $|f\rangle$, the energy separation between $|\alpha\rangle_v$ and $|\beta\rangle_v$ is larger for the symmetric state g than the antisymmetric state *u* because of the difference of the effective hybridization (Δ_g and Δ_u). The calculated stationary x-ray absorption [(a) and (b)] and optical absorption [(c) and (d)] spectra are shown in Fig. 3. Since the dipole approximation holds in the optical regime, only the symmetric states are active. As the excitonic effects becomes large [see (b) $U^{cb} = 4$ eV and (d) $U^{ba} = 4$ eV], the lower peak intensity grows.

The stationary resonant x-ray emission spectra for $\mathbf{q}_s = \mathbf{0}$ are shown in the left panel of Fig. 4. In this case, the final state must be the symmetric one due to the momentum selection rule. The solid (dotted) lines show spectra corresponding to the excitation x-ray energy tuned to the lower (higher) energy peak in the x-ray absorption spectrum, i.e., the incident x-ray energy is resonant with $|\alpha\rangle_c$ ($|\beta\rangle_c$). When (a) $U^{cb} = U^{ba} = 0$ eV, Eq. (20) gives $\theta = -\pi/4$, and Eqs. (18), (21), and (A4) show that only the transitions of $|\alpha\rangle_c \rightarrow |\alpha\rangle_v$ and $|\beta\rangle_c \rightarrow |\beta\rangle_v$ are allowed for $\mathbf{q}_s = \mathbf{0}$, as shown by the thick arrows in Fig. 2. This strict selection rule reflects the fact the spatial coherence of the core-hole states over both sites is maintained during the x-ray emission process. This has been experimentally demonstrated in the O 1*s* resonant x-ray emission spectrum of O_2. [40]

Coulomb interactions make the transitions $|\alpha\rangle_c \rightarrow |\beta\rangle_v$ and $|\alpha\rangle_c \rightarrow |\beta\rangle_v$ allowed, as shown by the thin arrows in Fig. 2. As U^{cb} is increased [Fig. 4(b)], the oscillator strength of the excitation to $|\alpha\rangle_c$ becomes large, and the emission peaks from $|\alpha\rangle_c$ (solid line) are dominant compared to $|\beta\rangle_c$ (dotted line). On the other hand, when $U^{cb} = 0$ eV and $U^{ba} = 4$ eV [Fig. 4(c)], the emission peaks from both $|\alpha\rangle_c$ and $|\beta\rangle_c$ have the same intensity, and a small satellite appears on the lower (or higher)-energy side of the principal transition.

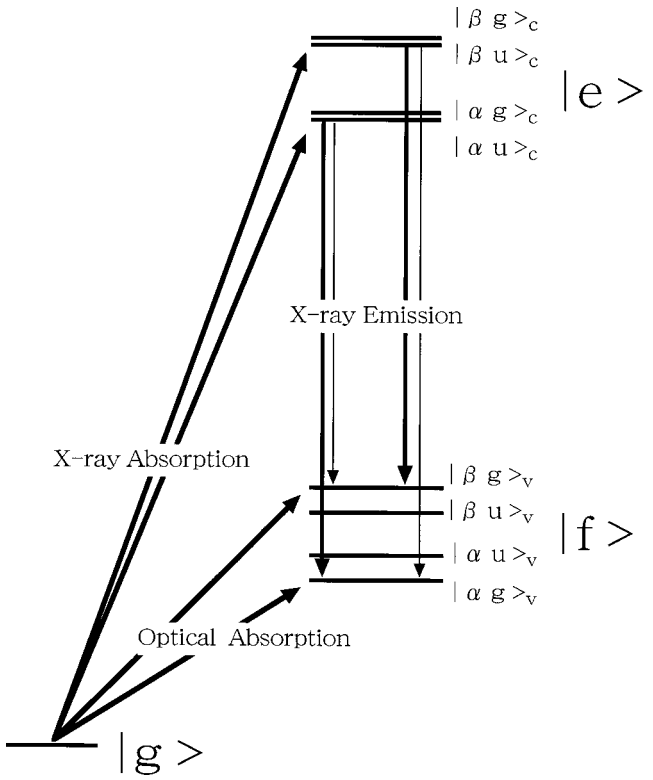

FIG. 2. Energy level scheme for the global eigenstates for $N = 2$ system. The x-ray absorption, optical absorption, and x-ray emission transitions are also shown here. The x-ray emission transitions for $\mathbf{q}_s = \mathbf{0}$, where only the symmetric final states are allowed. In the absence of excitonic couplings, only the x-ray emission transitions shown by the thick arrows are allowed.

To analyze the electron-hole dynamics underlying these spectra we consider the expectation values of the relative separation between the core hole and excited electron

$$s(t) \equiv \sum_{j=0,1} j P_j(t), \tag{23}$$

where $P_j(t)$ is the probability of finding core exciton with electron-hole separation *j* at time *t*,

$$P_j(t) \equiv \langle j,g(u)|\rho^{(2)}(t)|j,g(u)\rangle, \tag{24}$$

and $\rho^{(2)}(t)$ is the second-order density matrix defined in Eq. (7) in Ref. [53]. The inverse participation ratio is another useful measure of the degree of delocalization of the pair [58],

$$\kappa(t) \equiv 1 \Big/ \sum_j P_j^2(t). \tag{25}$$

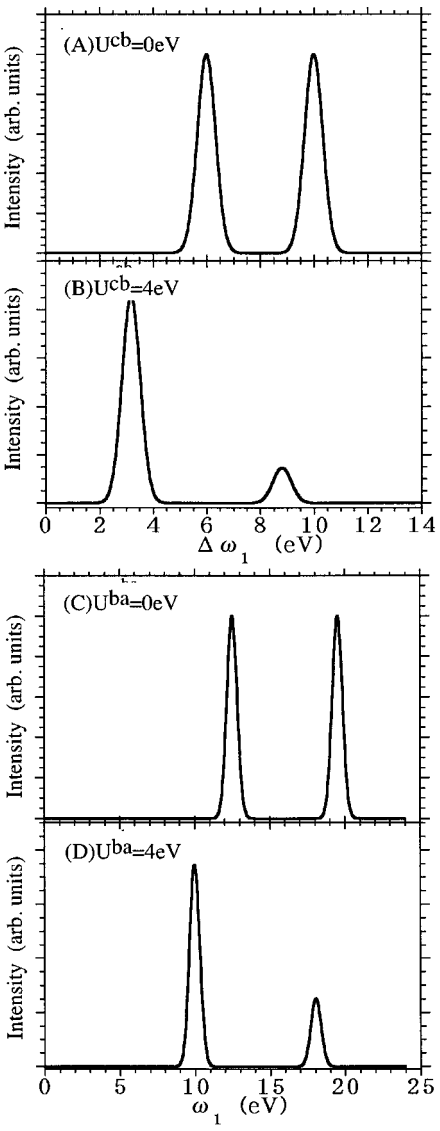

FIG. 3. Stationary x-ray absorption spectra for $N=2$, (a) $U^{cb}=0$ eV and (b) $U^{cb}=4$ eV, where $\Delta\omega_1$ denotes $\omega_1-\omega_0$. Optical absorption spectra are shown for (c) $U^{ba}=0$ eV and (d) $U^{ba}=4$ eV, where ω_1 denotes optical photon energy.

From the above definition, $s(t)$ is the first moment of the distribution of $P_j(t)$, while $\kappa(t)$ gives us the distribution width of $P_j(t)$. In Fig. 5 we display the time dependence of $s(t)$ and $\kappa(t)$. For (A)$U^{cb}=0$ eV, we note that the excited pair is maximally separated and then bounces back to the excited site periodically: Only when $\kappa(t)=1$ the density matrix $\rho^{(2)}(t)$ is diagonal with respect to the site index j and the core excited state is described as a pure state in the basis of $|j,g(u)\rangle$, otherwise the core-excited state is represented by a coherent sum of $|j,g(u)\rangle$, so that $s(t)$ takes a value between 0 and 1, e.g., when $\kappa(t)=2$ $s(t)=0.5$. For (b) $U^{cb}=4$ eV the excited electron is more strongly bound to the excited site, so that $s(t)$ never reaches to 1.

This relative electron-hole motion of the core- exciton is directly monitored in the TFXES. The calculated TFXES are depicted in Figs. 6(a)–6(c), for the same parameters of Fig. 4(a)–4(c), respectively. We further assumed $\delta_1=0.1$ fs and

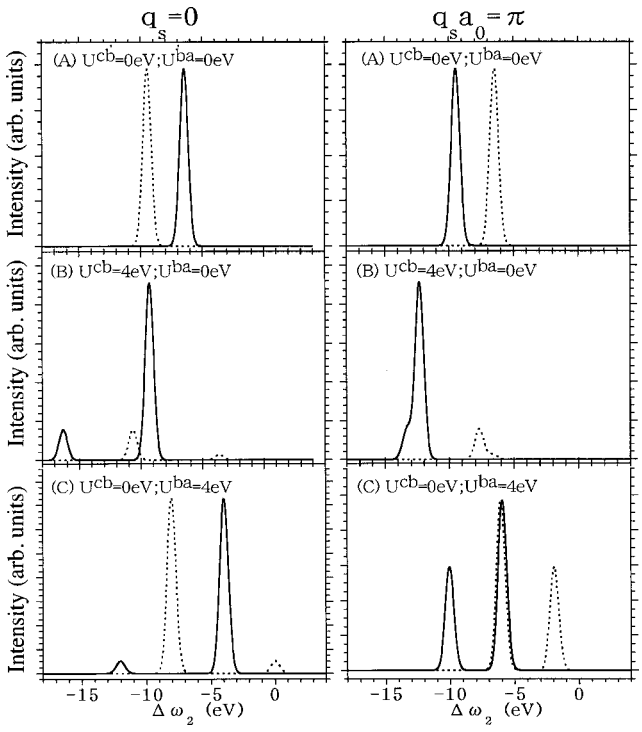

FIG. 4. Stationary resonant x-ray emission spectra for $N=2$. The left panel is the spectra for $\mathbf{q}_s=\mathbf{0}$; (a) $U^{cb}=U^{ba}=0$ eV, (b) $U^{cb}=4$ eV, $U^{ba}=0$ eV, and (c) $U^{cb}=0$ eV, $U^{ba}=4$ eV. The right panel is the spectra for $\mathbf{q}_s\cdot\mathbf{a}_0=\pi$; (a) $U^{cb}=U^{ba}=0$ eV, (b) $U^{cb}=4$ eV, $U^{ba}=0$ eV, and (c) $U^{cb}=0$ eV, $U^{ba}=4$ eV. $\Delta\omega_2$ denotes $\omega_2-\omega_0$, where ω_2 is a emitted x-ray photon energy. Solid (dotted) lines correspond to excitation energies tuned to the lower (higher) peaks of the x-ray absorptions in Fig. 3.

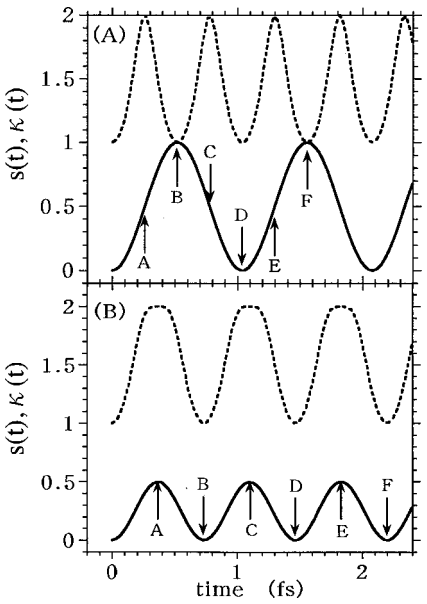

FIG. 5. The expectation values of the relative separation between the core hole and the excited electron $s(t)$ (solid lines) and the inverse participation ratio $\kappa(t)$ (dotted lines) for $N=2$: (a) $U^{cb}=0$ eV and (b) $U^{cb}=4$ eV.

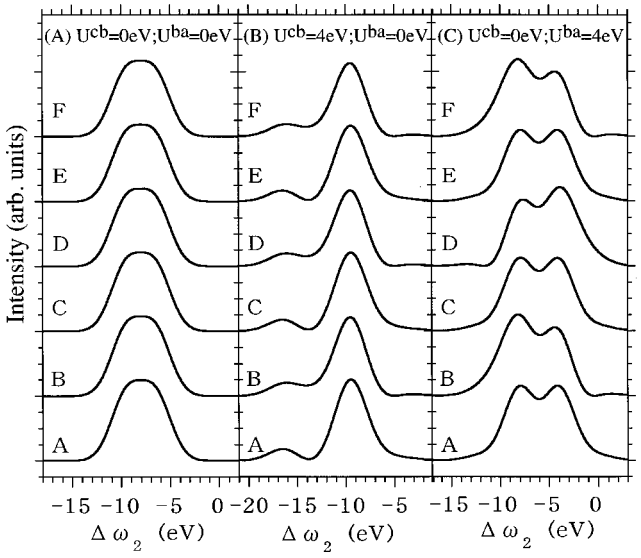

FIG. 6. TFXES for $N=2$ for $\mathbf{q}_s=\mathbf{0}$, where $\Delta\omega_2\equiv\omega_2-\omega_0$; (a) $U^{cb}=U^{ba}=0$ eV, (b) $U^{cb}=4$ eV, $U^{ba}=0$ eV, and (c) $U^{cb}=0$ eV, $U^{ba}=4$ eV. The delays τ of the time-gated pulse are given by the arrows in Fig. 5: In the left and the right panels the delay time *A* to *F* refer to the arrows in Fig. 5(a). In the middle panel the delay time A to F refer to the arrows in Fig. 5(b).

$\delta_t=0.3$ fs. The pulse lengths are taken to be shorter than the core hole lifetime (~ 10 fs), and the characteristic time for the exciton motion (see Fig. 5), but δ_t is still long enough to retain spectral structure in the x-ray emission. The delay times τ are shown by the arrows in Fig. 5.

When (a) $U^{cb}=U^{ba}=0$ eV, the two x-ray emission processes of $|g\rangle\rightarrow|\alpha\rangle_c\rightarrow|\alpha\rangle_v$ and $|g\rangle\rightarrow|\beta\rangle_c\rightarrow|\beta\rangle_v$ are independent, as indicated earlier and, the TFXES does not change with time. For large U^{cb} (b), the excited core-electron is bound by the core hole potential, forming the core exciton. The change of the TFXES with time, is too small to be noticeable. On the other hand, when U^{ba} becomes large while U^{cb} is left unchanged (c), the intensities of the lower and higher energy peaks changes periodically with time. We note that even in this case the total emission intensity (time resolved but frequency integrated) is decreased smoothly by the nonradiative Auger decay Γ.

When the core hole and excited electron are located on the same site [spectrum D in Fig. 6(c)], the x-ray emission energy increases by the valence exciton binding energy, while the x-ray emission decreases when the hole and electron are separated. We can compare the TFXES when the excited electron and core-hole is located on the same site with the instantaneous FXES obtained by reducing the core-hole lifetime so that the excited electron cannot move away from the excited site. The FXES for various values of Γ are shown in Fig. 7. As Γ is increased, the intensity of the higher energy peak is increased. The FXES for $\Gamma=5$ eV($\hbar/\Gamma=0.13$ fs) is similar to the spectrum *D* in Fig. 6(c). The enhancement of the higher energy domain is caused by quantum interference between two emission paths of $|g\rangle\rightarrow|\alpha\rangle_c\rightarrow|\alpha\rangle_v$ and $|g\rangle\rightarrow|\beta\rangle_c\rightarrow|\alpha\rangle_v$ [43].

We next turn to the wave-vector dependence of the spectra. The stationary resonant x-ray emission spectra for $\mathbf{q}_s\cdot\mathbf{a}_0=\pi$ are shown in the right panel of Fig. 4, for the same parameters used in the case of $\mathbf{q}_s=\mathbf{0}$. The solid (dotted) lines are obtained when the incident x-ray energy is tuned to the lower (higher)-energy peak in the x-ray absorption. In this case, the final state must be antisymmetric due to the momentum selection rule. When (a) $U^{cb}=U^{ba}=0$ eV, the emission (solid) line corresponding to the transition to $|\alpha,u\rangle_v$ appears on the lower-energy side of the dotted line corresponding to the transition to $|\beta,u\rangle_v$. As long as $U^{ba}=0$ eV, the energy separation between $|\alpha,u\rangle_v$ and $|\beta,u\rangle_v$ is small, $2\Delta_u=2(\Delta^b-\Delta^a)=1$ eV. As U^{cb} increases (b), the transition to $|\beta,u\rangle_v$ following the excitation to $|\alpha\rangle_c$ state becomes allowed, forming the small shoulder on the lower energy side of the peak (the solid line). In contrast, upon excitation to $|\beta\rangle_c$, the transition to $|\alpha,u\rangle_v$ becomes allowed, as shown by the small shoulder on the higher-energy side of the peak (dotted line). As U^{ba} is increased leaving $U^{cb}=0$ eV, the energy separation between $|\alpha,u\rangle_v$ and $|\beta,u\rangle_v$ $(U^{ba}+\sqrt{(U^{ba})^2+4\Delta_u^2})$ becomes large, and the small shoulder is then separated from the main peak, and its intensity increases (c).

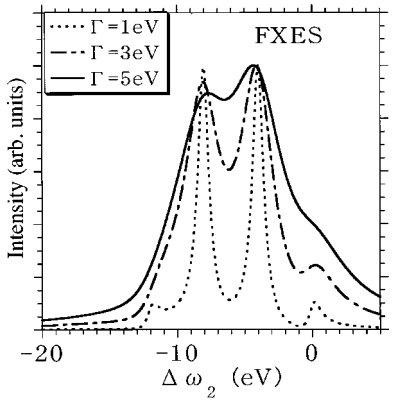

FIG. 7. FXES for $N=2$ for various values for the linewidth Γ.

The calculated TFXES for $\mathbf{q}_s\cdot\mathbf{a}_0=\pi$ with the same parameters of Fig. 4 are displayed in Fig. 8. While we can hardly see a large temporal evolution of the spectra in Figs. 8(a) and 8(b) for the same reasons on Figs. 6(a) and 6(b), the spectrum strongly changes with time for (c) $U^{cb}=0$ eV and $U^{ba}=4$ eV. In this case the satellite peaks corresponding to the $|\beta\rangle_c\rightarrow|\alpha,u\rangle_v$ and $|\alpha\rangle_c\rightarrow|\beta,u\rangle_v$ transitions [right panel (c) of Fig. 4] are stronger than in the case of $\mathbf{q}_s=\mathbf{0}$ [left panel (c) of Fig. 4]. The higher-energy peak that is attributed to the transition to the valence-exciton state ($|\alpha,u\rangle_v$) is therefore enhanced by the quantum interference between two emission paths of $|g\rangle\rightarrow|\alpha\rangle_c\rightarrow|\alpha\rangle_v$ and $|g\rangle\rightarrow|\beta\rangle_c\rightarrow|\alpha\rangle_v$, when the excited electron and core hole are located on the same site.

We next present calculations for a larger $N=16$ chain. We set $U^{cb}=U^{ba}=6$ eV and $\epsilon=0.8$ in Eq. (4). The x-ray absorption (a) and the optical absorption spectra (b) are shown in Fig. 9. The sharp $\omega_1=-0.98$ eV peak in Fig. 9(a) attributed to the transition to the strongly localized core-core exciton state, is followed by a progression of higher energy peaks corresponding to transitions to the delocalized core-excited states. Similarly the intense lowest energy peak in

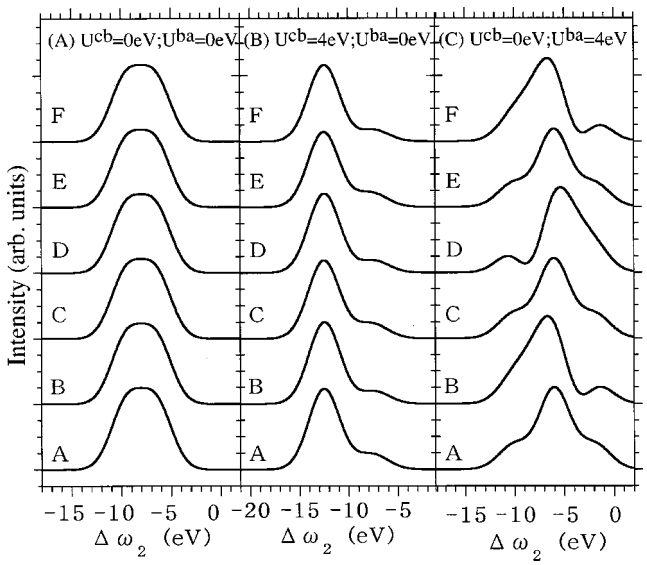

FIG. 8. TFXES for $N=2$ for $\mathbf{q}_s\cdot\mathbf{a}_0=\pi$; (a) $U^{cb}=U^{ba}=0$ eV, (b) $U^{cb}=4$ eV, $U^{ba}=0$ eV, and (c) $U^{cb}=0$ eV, $U^{ba}=4$ eV. The delay τ of the time-gated pulse corresponds to the arrows in Fig. 5: for (a) and (c) the delay time A to F is shown by to the arrows in Fig. 5(a), and for (b) the delay time A to F is shown by the arrows in Fig. 5(b).

Fig. 9(b) is due to the transition to the localized valence exciton state, and the higher-energy peaks are attributed to the delocalized valence-excited states.

The stationary resonant x-ray emission spectra for various scattering wave vectors are shown in the panels of (a) to (e) in Fig. 10 along with FXES. The incident x-ray energies are shown by the arrows (I–VII) in Fig. 9(a). Since the lifetime broadening $\Gamma=32$ meV is very small compared to the energy separations between core-excited eigenstates, FXES coincides with a sum of the stationary resonant x-ray emission spectra. It should be noted that we can probe the valence excitonic state with $\mathbf{q}_s\neq\mathbf{0}$ that is forbidden optically.

The most intense peak (I) in the calculated stationary resonant x-ray emission spectra is attributed to the transition from the strongly bound core exciton state to the bound valence exciton state. While the bound core exciton state has no energy dispersion due to the vanishing core-hole transfer integral, the bound valence exciton (Frenkel exciton) has a energy dispersion due to the translational motion. The strong wavevector dependence of the peak position of the spectrum (I) reflects the energy dispersion of the valence (Frenkel) exciton. When the incident energy is tuned to the higher-energy peaks in the x-ray absorption (II–VII), the main contribution comes from the transition from the spatially separated core exciton states to the spatially well-separated valence exciton states. Therefore the spectral change is similar to the case of $U^{ba}=U^{cb}=0$ eV (not shown).

The core-exciton motion in real space is illustrated in Fig. 9(c) that displays $s(t)$ and $\kappa(t)$. Because of the finite number of atoms in the system, $\kappa(t)$ undergoes periodic motion: a core hole and excited electron created at the same site, are then separated, and the excited core electron periodically comes close to the excited site.

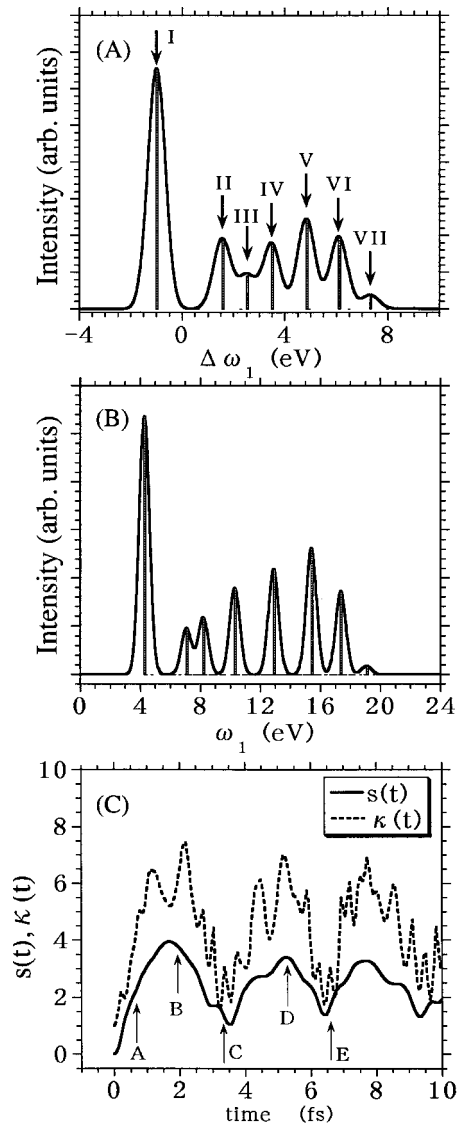

FIG. 9. (a) Stationary x-ray absorption and (b) optical absorption spectra for $N=16$. The expectation values of the relative separation between the core hole and the excited electron $s(t)$ (solid lines) and the inverse participation ratio $\kappa(t)$ (dotted lines) are shown in (c).

The TFXES for various $\mathbf{q}_s$ are shown in Figs. 11–13, where $\delta_1=0.2$ fs and $\delta_t=0.8$ fs. The centers of x-ray excitation energies ω_1 are shown by the arrows in Fig. 9(a). Fourier transform of the excitation x-ray pulse provides the half-width half-maximum in energy $\hbar/\delta_1\sqrt{2\ln 2}=3.87$ eV.

The TFXES depends both on the incident excitation energies and the scattering wave vectors similar to the stationary resonant x-ray emission spectra of Fig. 10, because the integration of the TFXES over the gated delay time τ for a particular excitation energy and a scattering wave vector corresponds to the stationary resonant x-ray emission spectrum for the same excitation energy and a scattering wave vector. However the temporal evolution of the TFXES strongly depend on the excitation energy. When the excitation energy is tuned around the core-exciton state [(I) and (II)], the excited electron is strongly bound around the excited site, and

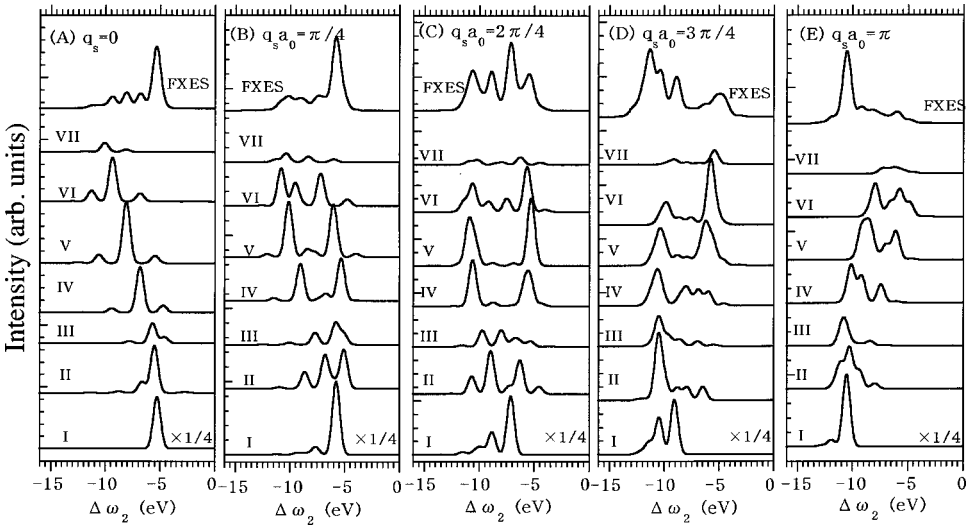

FIG. 10. Stationary resonant x-ray emission spectra for the various wave vector are shown in (a) to (e), where the excitation energies (I–VII) are shown by the arrows in x-ray absorption spectrum in Fig. 9(a).

the main contribution to the x-ray emission comes from the transition from the strongly bound core exciton to the strongly bound valence-exciton state. Since the x-ray emission takes place around a single atomic site, the TFXES does not depend on time. On the other hand, as the excitation energy is tuned around the center of the continuous absorption band [(IV)−(VI)], the exciton wave packet is created by the excitation x-ray pulse and the excited electron can hop among the atomic sites. The TFXES then changes periodically with time, reflecting the relative motion of the core-exciton [see Fig. 9(c)]. The temporal change of the TFXES together with the strong wave vector dependence and the excitation energy dependence, allow to directly probe and separate the relative and the translation motion of the exciton.

V. CONCLUDING REMARKS

In this paper we have formulated TFXES in terms of the nonlinear response functions computed using the sum-over states expression. When the excitation and time-gated pulses are well separated and in the absence of pure dephasing, the signal assumes a simple form as a sum of the eigenstates [Eq. (15)]. This theory was applied towards the real-time and real-space study of exciton motion in an atomic chain. TFXES along with the x-ray absorption, optical absorption, stationary resonant x-ray emission spectra, and the dynamical relative motion of the core exciton: $s(t)$, and $\kappa(t)$ were calculated. The relative motion of the core exciton has direct signatures in the TFXES showing a periodic change that traces the relative motion of the core exciton. When the ex-

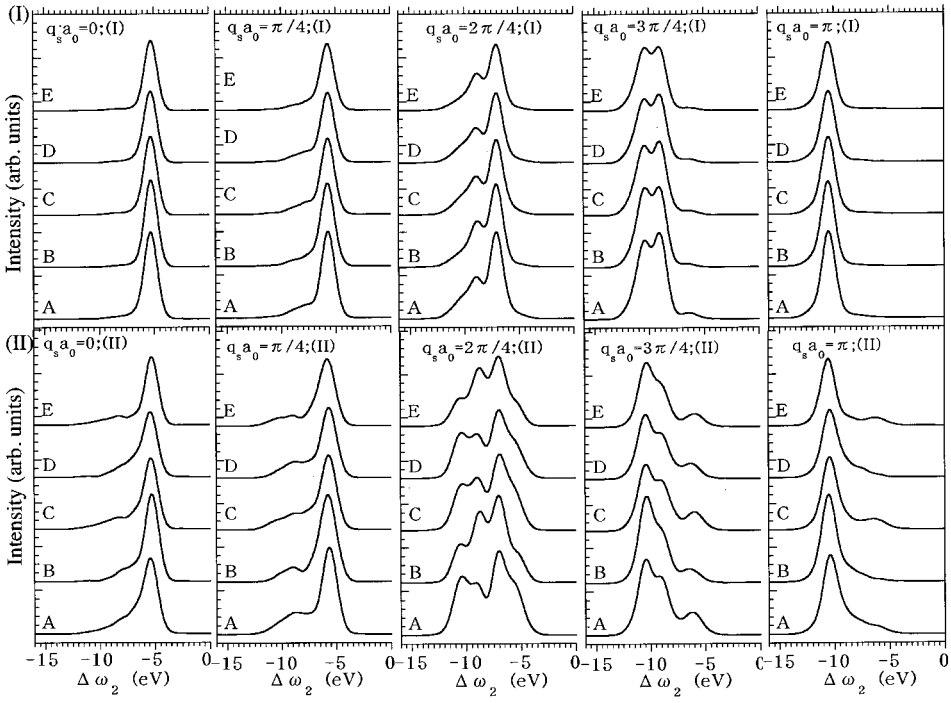

FIG. 11. TFXES for various scattering wave vectors for the excitation of (I) and (II) of Fig. 9.

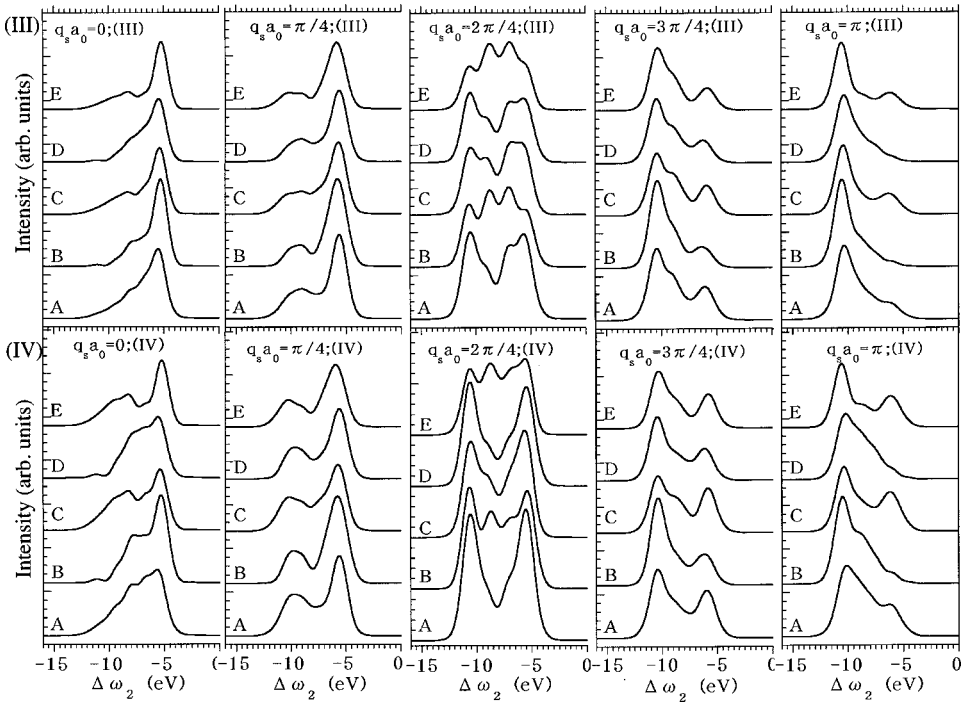

FIG. 12. TFXES for various scattering wave vectors for the excitation of (III) and (IV) of Fig. 9.

cited core electron and core hole are located on the same site the TFXES is consistent with the instantaneous FXES.

We have used typical parameters for linear conjugated molecules and assumed that the C 1*s* core electron is excited to an unoccupied state and x-ray emission by the electronic transition from the occupied valence state to the C 1*s* core state. Since the C 1*s* core hole lifetime is estimated to be 10 fs, we can detect the temporal change of the TFXES can be detected using a 0.6 fs x-ray-gated pulse. Many experiments and theoretical studies have suggested that in light atomic materials made out of B, C, N, and O, a large amplitude nuclear motion can be induced within the core-hole lifetime [38,40,47,49,59–61]. In this paper we only followed the motion of electron-hole pairs. However the nuclear motion induced by the core excitation in real-time and real-space with TFXES can be readily incorporated.

The double excitation of the valence exciton was neglected. When the energy gap between the valence and the conduction band is not so large, we have to take into account double excitations as well. The sum-over-state method then becomes tedious, because the number of the eigenstates rapidly grows. In order to take the many-body effects into ac-

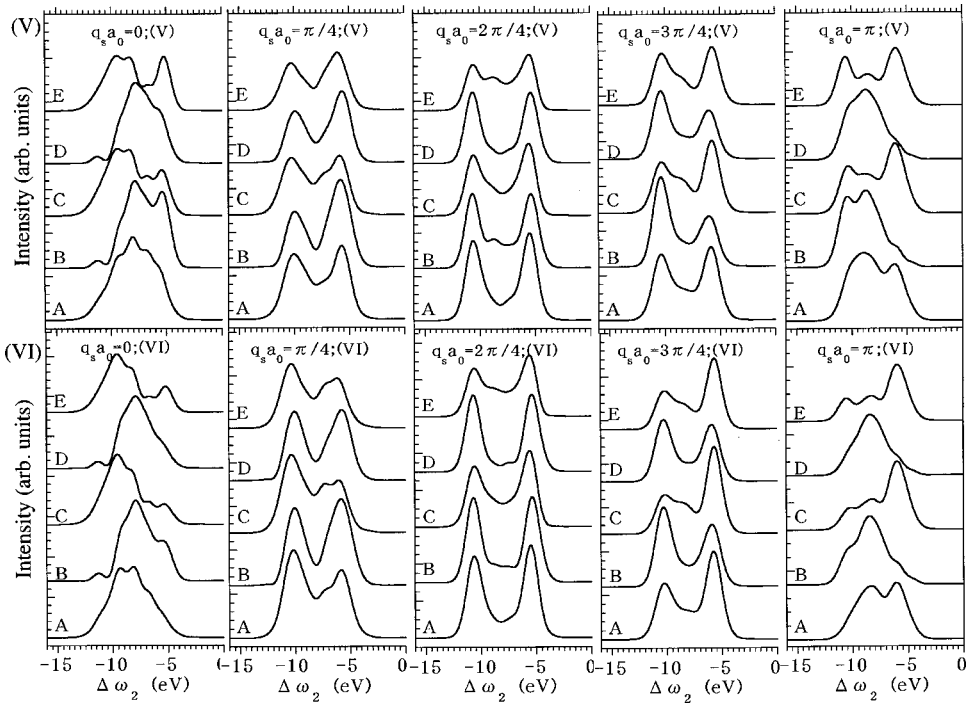

FIG. 13. TFXES for various scattering wave vectors for the excitation of (V) and (VI) of Fig. 9.

count, it may be preferable to directly follow the time evolution of the reduced density matrix using the time-dependent Hartree-Fock or time-dependent density-functional techniques [56,62–65] Other x-ray nonlinear spectroscopies, such as pump-probe and four-wave mixing, can be used to investigate the exciton dynamics. These spectroscopies which may be similarly formulated by nonlinear response functions, will be studied in the future.

ACKNOWLEDGMENTS

This work was partly supported by a Grant-in-Aid for Scientific Research from the Ministry of Education, Science, Sports, and Culture in Japan. We gratefully acknowledge the support of the National Science Foundation and the Petroleum Research Fund administered by the American Chemical Society.

APPENDIX A: THE GATED TFXES SIGNAL

In this appendix we derive Eq. (8).

The time-gated fluorescence obtained by mixing the signal with the time-gating field $A_t(t)$ is given by

$$\begin{aligned}F(\mathbf{k}_1,\mathbf{k}_2;\tau)=2\,\mathrm{Re}\int d\mathbf{r}\int d\mathbf{r}_3\int \mathbf{r}_2\int d\mathbf{r}_1\int_{-\infty}^{\infty}dt\int_0^{\infty}dt_3\int_0^{\infty}dt_2\int_0^{\infty}dt_1\\ \times\{A_1(t+\tau-t_1-t_2-t_3)A_1^*(t+\tau-t_2-t_3)A_t(t-t_3)A_t^*(t)\exp[i\omega_1 t_1+i\omega_2 t_3]\exp[i\mathbf{k}_1\cdot(\mathbf{r}_1-\mathbf{r}_2)]\\ \times\exp[i\mathbf{k}_2\cdot(\mathbf{r}_3-\mathbf{r})]R_1(\mathbf{r};\mathbf{r}_3\mathbf{r}_2\mathbf{r}_1t_3t_2t_1)+A_1^*(t+\tau-t_1-t_2-t_3)a_1(t+\tau-t_2-t_3)A_t(t-t_3)A_t^*(t)\\ \times\exp[-i\omega_1 t_1+i\omega_2 t_3]\exp[-i\mathbf{k}_1\cdot(\mathbf{r}_1-\mathbf{r}_2)]\exp[-i\mathbf{k}_2\cdot(\mathbf{r}-\mathbf{r}_3)]R_2(\mathbf{r};\mathbf{r}_3\mathbf{r}_2\mathbf{r}_1t_3t_2t_1)\\ +A_1^*(t+\tau-t_1-t_2-t_3)A_1(t+\tau-t_3)A_t(t-t_2-t_3)A_t^*(t)\exp[-i\omega_1 t_1-i(\omega_1-\omega_2)t_2+i\omega_2 t_3]\\ \times\exp[-i\mathbf{k}_1\cdot(\mathbf{r}_1-\mathbf{r}_3)]\exp[-i\mathbf{k}_2\cdot(\mathbf{r}-\mathbf{r}_3)]R_3(\mathbf{r};\mathbf{r}_3\mathbf{r}_2\mathbf{r}_1t_3t_2t_1)\}. \qquad \text{(A1)}\end{aligned}$$

R_1, R_2, and R_3 are the following four-point four-time correlation functions:

$$R_1=\langle\hat{j}(\mathbf{r}_2,t_1)\hat{j}(\mathbf{r}_3,t_1+t_2)\hat{j}(\mathbf{r},t_1+t_2+t_3)\hat{j}(\mathbf{r}_1,0)\rangle, \qquad \text{(A2a)}$$

$$R_2=\langle\hat{j}(\mathbf{r}_1,0)\hat{j}(\mathbf{r}_3,t_1+t_2)\hat{j}(\mathbf{r},t_1+t_2+t_3)\hat{j}(\mathbf{r}_2,t_1)\rangle, \qquad \text{(A2b)}$$

$$R_3=\langle\hat{j}(\mathbf{r}_1,0)\hat{j}(\mathbf{r}_2,t_1)\hat{j}(\mathbf{r},t_1+t_2+t_3)\hat{j}(\mathbf{r}_3,t_1+t_2)\rangle, \qquad \text{(A2c)}$$

where $\hat{j}(\mathbf{r},t)$ is the Heisenberg representation of the current density.

Using a localized basis set, we have

$$\begin{aligned}\int d\mathbf{r}\hat{j}(\mathbf{r})\exp[-i\mathbf{k}\cdot\mathbf{r}]&=\sum_l \exp[-i\mathbf{k}\cdot\mathbf{R}_l]\\ &\times(j_{bc}b_l^\dagger c_l^\dagger+j_{ac}a_l c_l^\dagger+\mathrm{H.c.}), \qquad \text{(A3a)}\\ &=\sum_l \exp[-i\mathbf{k}\mathbf{R}_l](\hat{j}(l)+\hat{j}^\dagger(l)), \qquad \text{(A3b)}\end{aligned}$$

where

$$\hat{j}(l)\equiv j_{bc}b_l^\dagger c_l^\dagger+j_{ac}a_l c_l^\dagger \qquad \text{(A4)}$$

between the core state c and the high energy state b or a:

$$j_{ia}=\frac{e}{m}\mathrm{Re}\int d\mathbf{r}\psi_i^*(\mathbf{r})\left(\frac{\hbar}{i}\nabla\psi_c(\mathbf{r})\right) \quad (i=b,a). \qquad \text{(A5)}$$

Combining Eqs. (A1), (A2), and (A3), we obtain Eq. (8).

APPENDIX B: DERIVATION OF EQ. (15)

Substituting Eqs. (9) and (12) into (8), we obtain for each Liouville pathway

$$\begin{aligned}F_1=2\pi^{-3/2}&\frac{1}{\delta_1\delta_2\sqrt{\delta_1^2+\delta_2^2}}\\ &\times\mathrm{Re}\sum_{gee'f}P(g)J_{fe;eg}(\mathbf{q}_s)J^*_{fe';e'g}(\mathbf{q}_s)\\ &\times\int_0^{\infty}dx\int_0^{\infty}dy\int_{|x-y|}^{\infty}dz\exp\left[-\frac{x^2}{\delta_1^2}+i2\omega_1 x\right]\\ &\times\exp\left[-\frac{y^2}{\delta_t^2}+i2\omega_2 y\right]\exp\left[-\frac{1}{\delta_1^2+\delta_t^2}\right.\\ &\left.\times(z-\tau)^2\right]I_{ef}(2y)I_{ee'}(z-x-y)I_{eg}(2x), \qquad \text{(B1a)}\end{aligned}$$

$$F_2 = 2\pi^{-3/2}\frac{1}{\delta_1\delta_2\sqrt{\delta_1^2+\delta_t^2}} \times \mathrm{Re}\sum_{gee'f} P(g)J_{fe;eg}(\mathbf{q}_s)J^*_{fe';e'g}(\mathbf{q}_s) \times \int_0^\infty dx\int_0^\infty dy\int_{|x-y|}^\infty dz\exp\left[-\frac{x^2}{\delta_1^2}-i2\omega_1 x\right] \times\exp\left[-\frac{y^2}{\delta_t^2}+i2\omega_2 y\right]\exp\left[-\frac{1}{\delta_1^2+\delta_t^2}\right. \times(z-\tau)^2\left.\right] I_{ef}(2y)I_{ee'}(z-x-y)I_{ge'}(2x) \quad \text{(B1b)}$$

$$F_3 = 2\pi^{-3/2}\frac{1}{\delta_1\delta_t\sqrt{\delta_1^2+\delta_t^2}}\mathrm{Re}\sum_{gee'f} P(g)J_{fe;eg}(\mathbf{q}_s)J^*_{fe';e'g}(\mathbf{q}_s) \times \int_0^\infty dx\int_0^\infty dy\int_{|x-y|}^\infty dz\exp\left[-\frac{x^2}{\delta_1^2}-i2\omega_1 x\right] \times\exp\left[-\frac{y^2}{\delta_t^2}+i2\omega_2 y\right]\exp\left[-\frac{1}{\delta_1^2+\delta_t^2}(z-\tau)^2\right] \times I_{ef}(z-x+y)I_{gf}(x+y-z)I_{ge'}(z+x-y). \quad \text{(B1c)}$$

Taking $\gamma_g=\gamma_f=0$ and $\hat{\Gamma}_{eg}=\hat{\Gamma}_{ee'}=\hat{\Gamma}_{ef}=0$, we obtain

$$\begin{aligned} &I_{ef}(2y)I_{ee'}(z-x-y)I_{ge'}(2x)\\ &\quad=I_{ef}(2y)I_{ee'}(z+x-y)I_{eg}(-2x)\\ &\quad=I_{ef}(z-x+y)I_{gf}(x+y-z)I_{ge'}(z+x-y). \end{aligned} \quad \text{(B2)}$$

Substituting Eq. (B2) into (B1), we can combine these three terms, and obtain Eq. (13).

If the incident x-ray pulse and the time-gated detection pulse are temporary well separated, we can extend the lower limit of the z integral to $-\infty$. The three-dimensional integrals in Eq. (13) can be factorized into three one-dimensional integrals, resulting in Eq. (15).

[1] V.F. Kamalov, I.A. Struganova, and K. Yoshihara, Chem. Phys. Lett. **213**, 7350 (1993).

[2] R. Gadanos, K.H. Feller, and A. Pugzlys, Opt. Commun. **112**, 157 (1994); E. Gaizanskas, K.H. Feller, and R. Gadanos, *ibid.* **118**, 360 (1995).

[3] K. Misawa, S. Machida, K. Horie, and T. Kobayashi, Chem. Phys. Lett. **240**, 210 (1995), K. Misawa and T. Kobayashi, Nonlinear Opt. **15**, 81 (1996), T. Kobayashi, Mol. Cryst. Liq. Cryst. Sci. Technol., Sect. A **283**, 17 (1996).

[4] V. Sundstrom and V. van Grondelle, in *Anoxygenic Photosynthetic Bacteria*, edited by R. E. Blankenship, M. T. Madiga, and C. E. Baner (Kluwer Academic, Dordrecht, 1995), p.349.

[5] V. van Grondelle, J. Dekker, T. Gillbro, and V. Sundstrom, Biochim. Biophys. Acta **1187**, 1 (1994).

[6] G. Bastard, *Wave Mechnics Applied to Semiconductor Heterostructures* (Les Editions de Phisique, Paris, 1988).

[7] H. Haug and S.W. Koch, *Quantum Theory of the Optical Electronic Properties of Semiconductors*, 3rd ed. (World Scientific, Singapore, 1994).

[8] L. Banyai and S.W. Koch, *Semiconductor Quantum Dots* (World Scientific, Singapore, 1993)

[9] *Optics of Semiconductor Nanostructures*, edited by F. Heneberger, S. Schmidt-Rink, and E.O. Gobel (Akademic Verlag, Berlin, 1993).

[10] A.P. Alivisatos, Science **271**, 933 (1996).

[11] S. Mukamel, Annu. Rev. Phys. Chem. **51**, 691 (2000), and references therein.

[12] A.H. Chin, R.W. Sconenlein, T.E. Glover, P. Baling, W.P. Leemans, and C.V. Shank, Phys. Rev. Lett. **83**, 336 (1999).

[13] V. Chernyak, N. Wang, and S. Mukamel, Phys. Rep. **263**, 213 (1995).

[14] T.S. Rose, R. Righini, and M.D. Fayer, Chem. Phys. Lett. **106**, 13 (1984).

[15] H.J. Eichler, P. Gunter, and D.W. Pohl, *Laser-Induced Dynamic Gratings* (Springer, Berlin, 1986).

[16] J. Knoester and S. Mukamel, Phys. Rep. **205**, 1 (1991).

[17] K. Siegbahn, C. Nordling, G. Johansson, J. Hedman, P. F. Heden, K. Hamrin, U. Gelius, T. Bergmark, L.O. Werme, R. Manne, and Y. Baer, *ESCA Applied to Free Molecules* (North-Holland, Amsterdam, 1969).

[18] *Handbook on Synchrotron Radiation* edited by G. V. Marr (North-Holland, Amsterdam, 1987).

[19] O. Gunnarsson and K. Schönhammer, Phys. Rev. B **28**, 4315 (1983).

[20] *Core-level Spectroscopy in Condensed Systems* edited by J. Kanamori and A. Kotani (Springer-Verlag, Berlin, 1988).

[21] J.J. Rehr and R.C. Albers, Rev. Mod. Phys. **72**, 621 (2000).

[22] D.C. Koningsberger, *X-ray Absorption: Principles, Applications, Techniques of EXAFS, SXAFS, and XANES* (New York, Willey, 1988).

[23] *Unoccupied Electronic States: Fundamentals for XANES, EELS, and BIS*, edited by J.C. Fuggle and J.E. Inglesfield (Springer-Verlag, Berlin, 1992).

[24] R. Jenkins, *X-ray fluorescence spectrometry* (Willey, New York, 1988).

[25] C.-O. Almbladh and L. Hedin, in *Handbook on Synchrotron Radiation*, edited by E. F. Koch (North-Holland, Amsterdam, Netherlands, 1983), p. 607.

[26] B. Roulet, J. Gavoret, and P. Nozieres, Phys. Rev. **178**, 1072 (1969), P. Nozieres, J. Gavoret, and B. Roulet, *ibid.* **178**, 1084 (1969), P. Nozieres, C.T. de Dominicis, *ibid.* **178**, 1097 (1969).

[27] G.D. Mahan, *Many-Particle Physics* (Plenum Press, New York, 1990).

[28] G.D. Mahan, Phys. Rev. B **15**, 4587 (1977).
[29] L.S. Cederbaum, J. Chem. Phys. **103**, 562 (1995).
[30] E. Pahl, H.D. Meyer and L.S. Cederbaum, Z. Phys. D: At., Mol. Clusters **38**, 215 (1996)
[31] F. Gel'mukhanov and H. Ågren, Phys. Rev. A **54**, 379 (1996).
[32] Y. Ma, K.E. Miyano, P.L. Cowan, Y. Aglitzkiy, and B.A. Karlin, Phys. Rev. Lett. **74**, 478 (1995).
[33] Y. Murakami, H. Kawada, H. Kawata, M. Tanaka, T. Arima, Y. Moritomo, and Y. Tokura, Phys. Rev. Lett. **80**, 1932 (1998).
[34] M.v. Zimmermann, J.P. Hill, D. Gibbs, M. Blume, D. Casa, B. Keimer, Y. Murakami, Y. Tomioka, and Y. Tokura, Phys. Rev. Lett. **83**, 4872 (1999).
[35] P. Abbamonte, C.A. Burns, E.D. Isaacs, P.M. Platzman, L.L. Miller, S.W. Cheong, and M.V. Klein, Phys. Rev. Lett. **83**, 860 (1999).
[36] K. Hamalainen, J.P. Hill, S. Huotari, C.-C. Kao, L.E. Berman, A. Kotani, T. Ide, J.L. Peng, and R.L. Greene, Phys. Rev. B **61**, 1836 (2000).
[37] Y. Tezuka, S. Shin, A. Agui, M. Fujisana, and T. Ishii, J. Phys. Soc. Jpn. **65**, 312 (1996).
[38] A. Cesar, F. Gel'mukhanov, Y. Luo, H. Ågren, P. Skytt, P. Glans, J. Guo, K. Gunnelin and J. Nordgren, J. Chem. Phys. **106**, 3439 (1997).
[39] L. Triguero, Y. Luo, L.G.M. Pettersson, H. Ågren, P. Vaterlein, M. Weinelt, A. Fohlisch, J. Hasselstrom, O. Karis, and A. Nilsson, Phys. Rev. B **59**, 5189 (1999).
[40] J. Nordgren, P. Glans, K. Gunnelin, J. Guo, P. Skytt, C. Sather and N. Wassdahl, Appl. Phys. **65**, 97 (1997).
[41] M. Magnuson, L. Yang, J.-H. Guo, C. Sathe, A. Agui, J. Nordgren, Y. Luo, A. Ågren, N. Johansson, W.R. Salancek, L.E. Horsburgh, and A.P. Monkman, J. Electron Spectrosc. Relat. Phenom. **101-103**, 573 (1999).
[42] M. van Veenendaal, P. Carra, and B.T. Thole, Phys. Rev. B **54**, 16 010 (1996).
[43] S. Tanaka and A. Kotani, J. Phys. Soc. Jpn. **61**, 4212 (1992).
[44] A. Kotani, J. Phys. Chem. **61**, 419 (2000)
[45] Y. Ma, Phys. Rev. B **49**, 5799 (1994).
[46] S. Ishiahara and S. Maekawa, Phys. Rev. B **58**, 13 442 (1998).
[47] S. Tanaka and Y. Kayanuma, Solid State Commun. **64**, 77 (1996).
[48] K. Okada and A. Kotani, J. Phys. Soc. Jpn. **69**, 3100 (2000).
[49] S.A. Malinovskaya and L.S. Cederbaum, Phys. Rev. A **61**, 042706 (2000).
[50] F. Gel'mukhanov, L.N. Mazalov, A.V. Nikolaev, and A.V. Kondratenko, Chem. Phys. Lett. **46**, 133 (1977).
[51] P. Salek, F. Gel'mukhanov, and H. Ågren, Phys. Rev. A **59**, 1147 (1999).
[52] F. Gel'mukhanov, P. Salek, A. Shalagin, and H. Ågren, J. Chem. Phys. **112**, 5593 (2000).
[53] S. Tanaka, V. Chernyak, and S. Mukamel, Phys. Rev. A **63**, 063405 (2001).
[54] B. Kempgens, H. Köppel, A. Kivimäki, M. Neeb, L.S. Cederbaum, and A.M. Bradshaw, Phys. Rev. Lett. **79**, 3617 (1997).
[55] A. Szabo and N.S. Ostlund, *Modern Quantum Chemistry: Introduction to Advanced Electronic Structure Theory* (McGraw-Hill, New York, 1989).
[56] S. Mukamel, *Principles of Nonlinear Spectroscopies* (Oxford University Press, New York, 1995).
[57] E.J. McGuire, Phys. Rev. **185**, 1 (1969). The estimated 10.3-fs C $1s$ core-hole lifetime reported in this work gives $\Gamma = 64$ meV.
[58] S. Mukamel and H. X. Wang, in *Optics of Semiconductor Nanostructures* edited by F. Henneberger, S. Schmidtt-Rink, and E. O. Gobel (Akademie Verlag, Berlin, 1993) p. 361.
[59] S. Tanaka, K. Ueda, and Y. Kayanuma, Phys. Rev. A **57**, 3437 (1998).
[60] M. Simon, C. Miron, N. Leclercq, P. Morin, K. Ueda, Y. Sato, S. Tanaka, and Y. Kayanuma, Phys. Rev. Lett. **79**, 3857 (1997).
[61] K. Ueda, J. Electron. J. Electron Spectrosc. Relat. Phenom. **88-91**, 1 (1998).
[62] V. Chernyak and S. Mukamel, J. Chem. Phys. **108**, 5812 (1996).
[63] S. Tretiak, V. Chernyak, and S. Mukamel, Int. J. Quantum Chem. **70**, 711 (1998).
[64] F. Gel'mukhanov, L. Yang, and H. Ågren, J. Chem. Phys. **105**, 5224 (1996v).
[65] P.M. Platzman and E.D. Isaacs, Phys. Rev. B **57**, 11 107 (1998).